

Late Pleistocene climate drivers of early human migration

Axel Timmermann^{1,2} & Tobias Friedrich¹

On the basis of fossil and archaeological data it has been hypothesized that the exodus of *Homo sapiens* out of Africa and into Eurasia between ~50–120 thousand years ago occurred in several orbitally paced migration episodes^{1–4}. Crossing vegetated pluvial corridors from northeastern Africa into the Arabian Peninsula and the Levant and expanding further into Eurasia, Australia and the Americas, early *H. sapiens* experienced massive time-varying climate and sea level conditions on a variety of timescales. Hitherto it has remained difficult to quantify the effect of glacial- and millennial-scale climate variability on early human dispersal and evolution. Here we present results from a numerical human dispersal model, which is forced by spatiotemporal estimates of climate and sea level changes over the past 125 thousand years. The model simulates the overall dispersal of *H. sapiens* in close agreement with archaeological and fossil data and features prominent glacial migration waves across the Arabian Peninsula and the Levant region around 106–94, 89–73, 59–47 and 45–29 thousand years ago. The findings document that orbital-scale global climate swings played a key role in shaping Late Pleistocene global population distributions, whereas millennial-scale abrupt climate changes, associated with Dansgaard–Oeschger events, had a more limited regional effect.

Numerous studies^{5–7} have postulated that human dispersal and evolution were a direct consequence of orbital-scale climate shifts

(Fig. 1b–d) during the Late Pleistocene (126–11 thousand years ago (ka)) and the Holocene (11–0 ka). Every ~21 thousand years decreased precession (Fig. 1a) and corresponding higher boreal summer insolation intensified rainfall in northern Africa, the Arabian Peninsula and the Levant⁸, thus generating habitable savannah-type corridors^{1,2} for *H. sapiens* and a possible exchange pathway between African and Eurasian populations, which in turn impacted the subsequent global dispersal pattern and gene flow of *H. sapiens* across Asia, Europe, Australia and into the Americas.

Elucidating the response of *H. sapiens* dispersal to past climate shifts has been hindered by the sparseness of palaeoenvironmental data in key regions⁴ such as northeastern Africa, the Levant and the Arabian Peninsula, by regional uncertainties of global climate model simulations (see Methods, Extended Data Fig. 3), and by the prevailing dating uncertainties of fossil or archaeological records. Here we set out to quantify the effects of climate on human dispersal over the last glacial period, using a numerical reaction/diffusion human dispersal model (HDM, see Methods, Extended Data Fig. 1), which is forced by time-varying temperature, net primary production, desert fraction (Extended Data Figs 4–6) and sea level boundary conditions (Fig. 1f) obtained from a transient glacial/interglacial global earth system model simulation⁹ covering the last 125 ka, an estimate of millennial-scale variability and sea level reconstructions¹⁰, respectively (see Methods). The LOVECLIM climate model used here (see Methods)

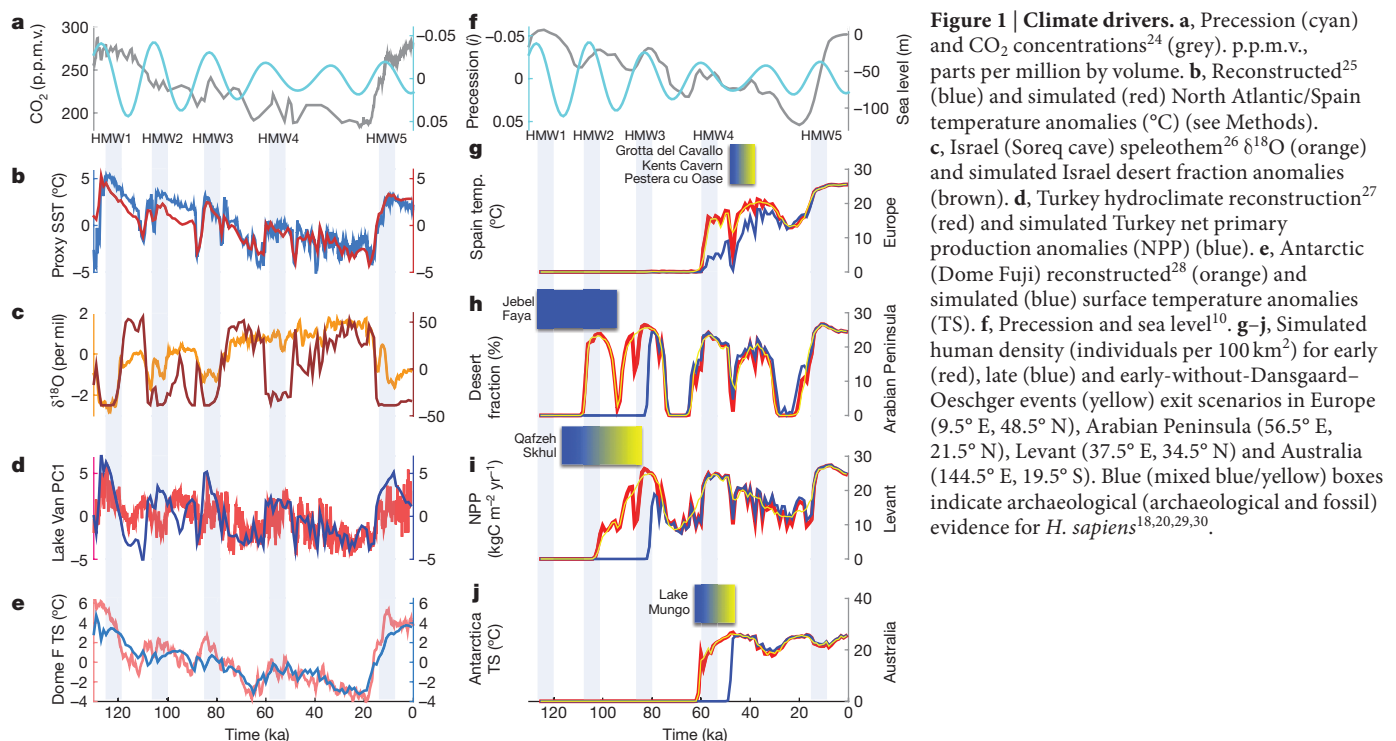


Figure 1 | Climate drivers. **a**, Precession (cyan) and CO₂ concentrations²⁴ (grey), p.p.m.v., parts per million by volume. **b**, Reconstructed²⁵ (blue) and simulated (red) North Atlantic/Spain temperature anomalies (°C) (see Methods). **c**, Israel (Soreq cave) speleothem²⁶ δ¹⁸O (orange) and simulated Israel desert fraction anomalies²⁷ (brown). **d**, Turkey hydroclimate reconstruction²⁷ (red) and simulated Turkey net primary production anomalies (NPP) (blue). **e**, Antarctic (Dome Fuji) reconstructed²⁸ (orange) and simulated (blue) surface temperature anomalies (TS). **f**, Precession and sea level¹⁰. **g–j**, Simulated human density (individuals per 100 km²) for early (red), late (blue) and early-without-Dansgaard–Oeschger events (yellow) exit scenarios in Europe (9.5° E, 48.5° N), Arabian Peninsula (56.5° E, 21.5° N), Levant (37.5° E, 34.5° N) and Australia (144.5° E, 19.5° S). Blue (mixed blue/yellow) boxes indicate archaeological (archaeological and fossil) evidence for *H. sapiens*^{18,20,29,30}.

¹International Pacific Research Center, University of Hawaii at Manoa, Honolulu, Hawaii 96822, USA. ²Department of Oceanography, University of Hawaii at Manoa, Honolulu, Hawaii 96822, USA.

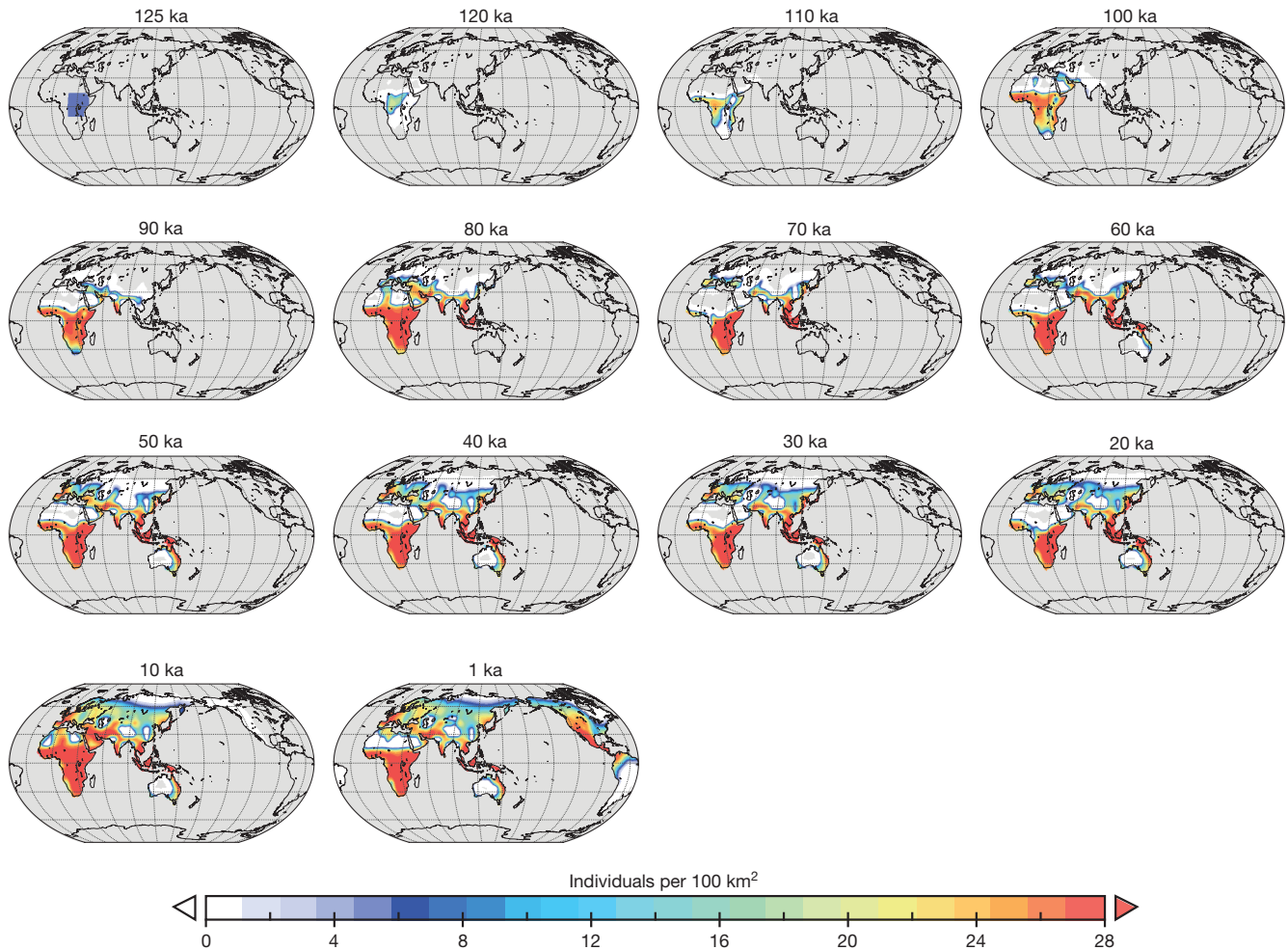


Figure 2 | Late Pleistocene human dispersal. Snapshots of the simulated evolution of human density (individuals per 100 km²) over the past 125 thousand years using the parameters of scenario A (early exit) experiment (see Methods) with full climate (orbital- and millennial-scale) and sea level forcing and with human adaptation (see Methods).

simulates glacial temperature and hydroclimate variability in good agreement with some palaeoclimate proxy data⁹ (Fig. 1b–e, Extended Data Fig. 2).

The first climate-forced HDM experiment (scenario A, Extended Data Tables 1, 2) covers the time evolution of the past 125 ka (Fig. 2, Supplementary Video 1) and accounts for a numerical representation of gradual human adaptation to environmental conditions (see Methods). Diffusing into vegetated regions, the first low-density migration wave of *H. sapiens* reaches the coastline of northeast Africa and the Bab-el-Mandeb around 115–106 ka (Figs. 1h, 2, Supplementary Video 1). Two rapid dispersals through the migration-favourable anomalously wet Arabian Peninsula- and Sinai-corridors (Fig. 1c, d, h, i, Extended Data Fig. 4) occur between 107–95 and 90–75 ka. Very low densities are simulated for Southern Europe from 95–72 ka (Fig. 2). The subsequent dry conditions during the period 71–60 ka (Marine Isotope Stage 4, MIS4) (Fig. 1c, d, Extended Data Figs 5, 6) cut off the exchange between the populations in northeastern Africa, and the rapidly eastward-spreading group in southern Asia (Fig. 2). This is in stark contrast to previous suggestions¹¹ of a very active migration corridor through the southern Arabian Peninsula during this time. During the subsequent precession minimum (increased boreal summer insolation) around 60–47 ka (Fig. 1a), simulated rainfall enhances net primary production in northern Africa, the Levant and the Arabian Peninsula (Extended Data Fig. 5) and a second prominent migration wave leaves northern Africa (Fig. 1h, i, 2). The onset of this

prominent wave around 60 ka (Fig. 1g) coincides with the youngest estimates of the L3-haplogroup-based age range for the time to most recent common ancestor (TMRCAs) of 79–60 ka^{11,12} and the subsequent emergence of mitochondrial DNA (mtDNA) haplogroups M, N and R. Eventually, this wave merges with the Eurasian population and leads to a boost of population density across Europe (Fig. 1g) and southern Asia. Meanwhile, *H. sapiens* cross the sea-level-altered Indonesian archipelago and arrive in Papua New Guinea and Australia around 60 ka (Figs. 1j, 2). For the subsequent period from 60–30 ka (MIS3) the model simulates a continuous Africa/Eurasia exchange of *H. sapiens* through the Levant (Fig. 1i) and an additional wave (45–30 ka) across the Bab-el-Mandeb and through the Arabian Peninsula (Fig. 1h). The dispersal across the Levant region is further modulated by the millennial-scale drought/pluvial variability associated with Dansgaard–Oeschger stadial/interstadial transitions (Fig. 1d, i). Completing the simulated grand journey from Africa to the Americas, *H. sapiens* cross the Bering land bridge into North America during the short period from 14–10 ka. With rising sea levels the Bering land bridge gets inundated during the glacial termination (Supplementary Video 1), thus terminating the geographic connectivity between Asia and North America.

According to this early exit scenario the first *H. sapiens* arrived in Europe, India and Southeast Asia and southern China in low densities (<5 individuals per 100 km²) already between 100–70 ka (see Supplementary Video 1, Fig. 3a). Whereas the simulated

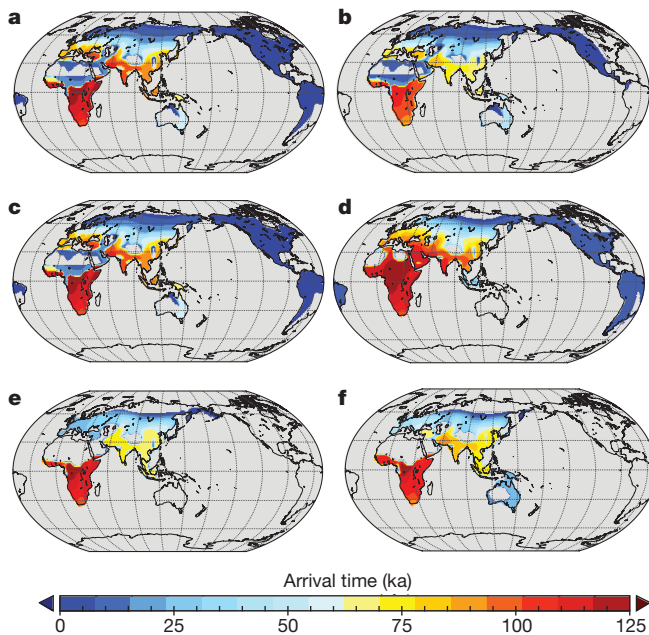


Figure 3 | Arrival Times for different dispersal scenarios. a–f. Time (ka) since last continuous human settlement for time-varying climate conditions following the transient scenario A simulation (early exit scenario) (a); scenario B (late exit scenario) (b); scenario A without Dansgaard–Oeschger variability (c); and for transient 125 ka simulations which use idealized constant climate forcing corresponding to 105 ka (d), 70 ka (e) and 21 ka (f) (see Extended Data Table 2 for more details).

early arrival of *H. sapiens* in Asia is consistent with previous findings^{13–15}, it appears to be at odds with a different interpretation of genetic and archaeological data¹⁶. Furthermore, the simulated low-density arrival of *H. sapiens* in Europe around 90–80 ka (Fig. 2) and the subsequent population increase from 60–50 ka challenges fossil and archaeological evidence¹⁷ placing the European arrival of *H. sapiens* before or around 45 ka. A possible explanation for this large discrepancy between model and observational evidence could be that the small populations of *H. sapiens* arriving in southeastern Europe after Human Migration Window (HMW) 3 may have been assimilated by the prevalent Neanderthal population and that only the subsequent wave from the Levant (during HMW4, 60–47 ka) led to a gradual transition from a Neanderthal- to a *H. sapiens*-dominated population regime.

A second parameter scenario (scenario B, see Methods, Extended Data Tables 1, 2) was run with the HDM to quantify the effect of a potential late MIS5a/MIS4 exodus^{11,16} on the subsequent population dynamics (Fig. 3b, Extended Data Fig. 7, Supplementary Video 2). According to this scenario, dispersal from central Africa to north-eastern Africa is inhibited due the prevailing drought conditions in north Africa during 116–108.5 ka (MIS5d) and 91.5–84.5 ka (MIS5b) (Extended Data Figs 5–7, Supplementary Video 2) and the higher human temperature sensitivity chosen for this scenario. This period is followed by a very rapid dispersal from Africa into Eurasia across the Red Sea and Levant starting in 84 ka (Fig. 1h, i, Extended Data Fig. 7). For MIS4 low densities are simulated for the Levant, Arabian Peninsula, Southeast Asia and southeastern Europe (Extended Data Fig. 7). During HMW4 (60–47 ka, Fig. 1h) a second migration event takes place through the Arabian Peninsula and Levant and human densities increase in western Europe, the Middle East, India and Indonesia, partly due to local environmental conditions, partly due to an influx from other areas. This scenario resembles the late single southern exit model¹¹ and mtDNA evidence for haplogroup L3. Although this scenario explains qualitatively the reconstructed arrival times in India¹⁶, Europe¹⁸, Australia¹⁹, and North America (Fig. 3b,

Supplementary Video 2), it does not explain the early MIS5 presence of *H. sapiens* in the Levant²⁰, the Arabian Peninsula (Fig. 1g, h) and in southern China¹⁵.

Both scenario A and B clearly reveal the impact of Dansgaard–Oeschger variability on the desert fraction and habitability of the Levant region (Extended Data Figs 5, 6, Fig. 1i). Whereas Dansgaard–Oeschger temperature and net primary production effects (Extended Data Figs 4, 5) on European, Mediterranean and north African population density are visible (Fig. 1g), their overall effect on global human dispersal and arrival times is negligible, as demonstrated by repeating scenario A without Dansgaard–Oeschger variability (see Methods) (Fig. 1g–i, yellow line, Fig. 3c).

To better understand the effect of glacial climate variability on the Late Pleistocene global human dispersal compared to non-climatic effects, we conducted three additional highly idealized sensitivity experiments (see Methods). For these 125 ka-long simulations we ignore the presence of glacial/interglacial climate variability and the orbital forcing and just prescribe perpetual climate conditions for 105 ka (MIS5c), 70 ka (MIS4), and 21 ka (Last Glacial Maximum, LGM). Comparing the times of last continuous human settlement simulated by scenario A simulation (Fig. 3a) with the corresponding maps for the perpetual MIS5c, MIS4 and LGM experiments (Fig. 3d, e, f), we find substantial differences in the peopling pattern during the Late Pleistocene, which can be understood either in terms of the differences in global climate conditions or in terms of sea level.

Here we presented a numerical modelling framework to quantify the effects of past spatiotemporal climate and sea level change on the global migration patterns of *H. sapiens*. Consistent with the recently proposed early onset multiple dispersal model²¹ and supported by phenotype analyses of early human neurocranial geometries²², we found evidence for multiple climate-mediated MIS3–5 dispersal and mixing waves across the Africa/Asian nexus. Precession forcing served as a key pacemaker for these glacial events which occurred around 106–94 ka (HMW2), 89–73 ka (HMW3) and 59–47 ka (HMW4) and 45–29 ka and which may have also contributed to potential gene flow back into Africa²¹. The large 59–47 ka dispersal event through the Arabian Peninsula, simulated by the HDM as well as by a recent demographic model²³, probably left the most prominent genetic traces in the genome of non-African *H. sapiens*, thus linking it to the TMRCA, the main gene flow patterns and estimated ages of mtDNA markers M and N and of the Y chromosome haplogroups M174, M130 and M89. Whether mtDNA evidence can be used to unequivocally distinguish between the orbital pulsation scenario and the late single-exodus scenario needs to be further explored. In addition to the orbital-scale pacing of human dispersal, we found modelling evidence for the impact of millennial-scale variability on regional population densities (Fig. 1g, h). However, according to our simulations the effects of abrupt climate change on global population dynamics and the first arrival times were negligible (Fig. 3c).

Consistent with a plethora of recent studies^{14,15,21}, our early exit climate/human dispersal simulation reproduces an early MIS5 exodus of *H. sapiens* out of Africa and a rapid dispersal along the southern rim of Asia into southern China and eventually into Australia during MIS3 and MIS4 (Supplementary Video 1). Our model simulation also shows an almost synchronous early arrival in southern China and in Europe around 90–80 ka. Given this plausible scenario, it is perplexing that the first *H. sapiens* fossil in southern China pre-dates the oldest discovered fossils of *H. sapiens* in Europe by about 35–40 thousand years. This discrepancy could be reconciled by assuming that the northern route into Europe was much more influenced by the biological and cultural interaction between *H. sapiens* and Neanderthals¹⁷ than the southern route into Asia.

Online Content Methods, along with any additional Extended Data display items and Source Data, are available in the online version of the paper; references unique to these sections appear only in the online paper.

Received 7 January; accepted 12 August 2016.

Published online 21 September 2016.

- Jennings, R. P. *et al.* The greening of Arabia: Multiple opportunities for human occupation of the Arabian Peninsula during the Late Pleistocene inferred from an ensemble of climate model simulations. *Quat. Int.* **382**, 181–199 (2015).
- Parton, A. *et al.* Orbital-scale climate variability in Arabia as a potential motor for human dispersals. *Quat. Int.* **382**, 82–97 (2015).
- Larrasoana, J. C., Roberts, A. P. & Rohling, E. J. Dynamics of green Sahara periods and their role in hominin evolution. *PLoS One* **8**, e76514 (2013).
- Breeze, P. S. *et al.* Palaeohydrological corridors for hominin dispersals in the Middle East similar to 250–70,000 years ago. *Quat. Sci. Rev.* **144**, 155–185 (2016).
- Carto, S. L., Weaver, A. J., Hetherington, R., Lam, Y. & Wiebe, E. C. Out of Africa and into an ice age: on the role of global climate change in the late Pleistocene migration of early modern humans out of Africa. *J. Hum. Evol.* **56**, 139–151 (2009).
- Castañeda, I. S. *et al.* Wet phases in the Sahara/Sahel region and human migration patterns in North Africa. *Proc. Natl Acad. Sci. USA* **106**, 20159–20163 (2009).
- Scholz, C. A. *et al.* East African megadroughts between 135 and 75 thousand years ago and bearing on early-modern human origins. *Proc. Natl Acad. Sci. USA* **104**, 16416–16421 (2007).
- Frumkin, A., Bar-Yosef, O. & Schwarcz, H. P. Possible paleohydrologic and paleoclimatic effects on hominin migration and occupation of the Levantine Middle Paleolithic. *J. Hum. Evol.* **60**, 437–451 (2011).
- Timmermann, A. *et al.* Modeling Obliquity and CO₂ Effects on Southern Hemisphere Climate during the Past 408 ka. *J. Clim.* **27**, 1863–1875 (2014).
- Waelbroeck, C. *et al.* Sea-level and deep water temperature changes derived from benthic foraminifera isotopic records. *Quat. Sci. Rev.* **21**, 295–305 (2002).
- Oppenheimer, S. Out-of-Africa, the peopling of continents and islands: tracing uniparental gene trees across the map. *Phil. Trans. R. Soc. Lond. B* **367**, 770–784 (2012).
- Soares, P. *et al.* The Expansion of mtDNA Haplogroup L3 within and out of Africa. *Mol. Biol. Evol.* **29**, 915–927 (2012).
- Petraglia, M. *et al.* Middle Paleolithic assemblages from the Indian subcontinent before and after the Toba super-eruption. *Science* **317**, 114–116 (2007).
- Petraglia, M. D., Haslam, M., Fuller, D. Q., Boivin, N. & Clarkson, C. Out of Africa: new hypotheses and evidence for the dispersal of *H. sapiens* along the Indian Ocean rim. *Ann. Hum. Biol.* **37**, 288–311 (2010).
- Liu, W. *et al.* The earliest unequivocally modern humans in southern China. *Nature* **526**, 696–699 (2015).
- Mellars, P., Gori, K. C., Carr, M., Soares, P. A. & Richards, M. B. Genetic and archaeological perspectives on the initial modern human colonization of southern Asia. *Proc. Natl Acad. Sci. USA* **110**, 10699–10704 (2013).
- Benazzi, S. *et al.* Early dispersal of modern humans in Europe and implications for Neanderthal behaviour. *Nature* **479**, 525–528 (2011).
- Fu, Q. *et al.* An early modern human from Romania with a recent Neanderthal ancestor. *Nature* **524**, 216–219 (2015).
- Clarkson, C. *et al.* The archaeology, chronology and stratigraphy of Madjedbebe (Malakunanja II): A site in northern Australia with early occupation. *J. Hum. Evol.* **83**, 46–64 (2015).
- Grün, R. *et al.* U-series and ESR analyses of bones and teeth relating to the human burials from Skhul. *J. Hum. Evol.* **49**, 316–334 (2005).
- Groucutt, H. S. *et al.* Rethinking the dispersal of *H. sapiens* out of Africa. *Evol. Anthropol.* **24**, 149–164 (2015).
- Gunz, P. *et al.* Early modern human diversity suggests subdivided population structure and a complex out-of-Africa scenario. *Proc. Natl Acad. Sci. USA* **106**, 6094–6098 (2009).
- Eriksson, A. *et al.* Late Pleistocene climate change and the global expansion of anatomically modern humans. *Proc. Natl Acad. Sci. USA* **109**, 16089–16094 (2012).
- Lüthi, D. *et al.* High-resolution carbon dioxide concentration record 650,000–800,000 years before present. *Nature* **453**, 379–382 (2008).
- Martrat, B. *et al.* Four climate cycles of recurring deep and surface water destabilizations on the Iberian margin. *Science* **317**, 502–507 (2007).
- Bar-Matthews, M., Ayalon, A., Kaufman, A. & Wasserburg, G. J. The Eastern Mediterranean paleoclimate as a reflection of regional events: Soreq cave, Israel. *Earth Planet. Sci. Lett.* **166**, 85–95 (1999).
- Stockhecke, M. *et al.* Millennial to orbital-scale variations of drought intensity in the Eastern Mediterranean. *Quat. Sci. Rev.* **133**, 77–95 (2016).
- Kawamura, K. *et al.* Northern Hemisphere forcing of climatic cycles in Antarctica over the past 360,000 years. *Nature* **448**, 912–916 (2007).
- Armitage, S. J. *et al.* The southern route “out of Africa”: evidence for an early expansion of modern humans into Arabia. *Science* **331**, 453–456 (2011).
- Higham, T. *et al.* The earliest evidence for anatomically modern humans in northwestern Europe. *Nature* **479**, 521–524 (2011).

Supplementary Information is available in the online version of the paper.

Acknowledgements We thank S. Feakins, M. Segsneider and Y. Chikamoto for discussions and L. Menviel for providing the data of the LOVECLIM Dansgaard-Oeschger hindcast experiment, A. Ganopolski for providing the ice-sheet forcing from CLIMBER and M. Tigchelaar for providing the PMIP3 model data. A.T. is supported through the US NSF (grants 1341311, 1400914).

Author Contributions A.T. designed the research study, wrote the numerical model code for the human dispersal model, conducted the human dispersal numerical experiments and wrote the paper. T.F. ran the transient climate model simulation, conducted the model/proxy data comparison and contributed to the interpretation of the data.

Author Information The climate model and human dispersal model data are available on <http://apdrc.soest.hawaii.edu/projects/HDM>. Reprints and permissions information is available at www.nature.com/reprints. The authors declare no competing financial interests. Readers are welcome to comment on the online version of the paper. Correspondence and requests for materials should be addressed to A.T. (axel@hawaii.edu).

Reviewer Information *Nature* thanks P. deMenocal, R. Jennings, M. Petraglia and the other anonymous reviewer(s) for their contribution to the peer review of this work.

METHODS

No statistical methods were used to predetermine sample size. The experiments were not randomized and the investigators were not blinded to allocation during experiments and outcome assessment.

HDM equations and climate forcing. To simulate human migration out of Africa and its subsequent global dispersal under time-varying climate conditions we employ a reaction/diffusion model for human density $\rho(x,y,t)$ in each grid point (x,y) and at time t . Similar models, also known as modified Fisher–Kolmogorov or Fisher–Skellam models have been used in previous idealized human dispersal modelling studies^{31,32}. In our HDM the reaction terms (growth G and mortality M) are dependent on three key vegetation, climate parameters: net primary productivity $N(x,y,t)$, which controls the availability of carbon-based food sources, desert fraction $d(x,y,t)$ and temperature $T(x,y,t)$, which are interpreted here as key climate stressors that determine the mortality of *H. sapiens*. Furthermore, a quadratic mortality term is included to avoid exponential growth during the simulation. The governing equation for $\rho(x,y,t)$ reads:

$$\frac{\partial \rho}{\partial t} = K \nabla^2 \rho + \Gamma [N(x,y,t)] \rho - M[d(x,y,t), T(x,y,t)] \rho - \alpha \rho^2 \quad (1)$$

The growth rate of human density is parameterized as a function of net primary productivity $N(x,y,t)$ in terms of $\Gamma(N) = \gamma \{0.5 \tanh[(N - N_c)/N_w] + 0.4\}$. Assuming that the early human diet consisted largely of grazing mammals, this equation captures the notion that the primary productivity in each model grid box is linked to the edible biomass. A net primary productivity N_c is required in each grid box to maintain human population. We make the assumption that the mortality rate in each grid box is strongly controlled by the desert fraction d and the annual mean surface temperatures T . Climates with temperature below T_c will abruptly increase human mortality. Furthermore, we include a dependence of M on the desert fraction d . Human mortality will increase rapidly—a result of sparse food and water resources—if the desert fraction increases beyond d_c . Both factors are parameterized as: $M(d,t) = \mu \max\{1 + \tanh[(d - d_c)/d_w], 1.67[1 - \tanh[(T - T_c)/T_w]]\}$. The explicit equations used here for growth and mortality differ from the simplified logistic growth law used in previous studies³³.

Coastal express. For coastal points, we assume an alongshore advection with a mean alongshore velocity U_p (see Supplementary Table 1). The time evolution of ρ is then calculated from:

$$\frac{\partial \rho}{\partial t} = -U_p \cdot \nabla \rho + \Gamma [N(x,y,t)] \rho - M[d(x,y,t), T(x,y,t)] \rho - \alpha \rho^2$$

Accelerated migration along rivers³⁴ is not taken into account. The simulated human dispersal represents a strongly idealized scenario, which does not include competition or assimilation with *H. neanderthalensis*, *H. erectus* or Denisovans. To extend the model to a more realistic multi-actor framework would require more detailed information on the respective climate sensitivities and better observational constraints on the initial population densities.

Island hopping. Short-distance sea-faring is parameterized as a Gaussian decay away from the coast with a width of 1° .

Numerical implementation. The HDM is discretized using a first order upwind in time and second order central difference in space method. Our numerical implementation uses a $1^\circ \times 1^\circ$ horizontal grid with a time-step of 1 year. The physical model parameters chosen here are listed in Extended Data Table 1.

Orbital-scale simulation. To study the effects of slowly evolving glacial boundary conditions on the climate system and human dispersal we conducted a transient glacial–interglacial climate model simulation with the earth system model LOVECLIM (abbreviated as SIM). The simulation SIM is based on the earth system model LOVECLIM³⁵, version 1.1. The atmospheric component of the coupled model LOVECLIM is ECBilt³⁶, a spectral T21, three-level model, based on quasi-geostrophic equations extended by estimates of ageostrophic terms. The model contains a full hydrological cycle, which is closed over land by a bucket model for soil moisture and a runoff scheme. Diabatic heating due to radiative fluxes, the release of latent heat and the exchange of sensible heat with the surface are parameterized. The ocean–sea ice component of LOVECLIM, CLIO³⁷ consists of a free-surface Ocean General Circulation Model with $3^\circ \times 3^\circ$ resolution coupled to a thermodynamic–dynamic sea ice model. Coupling between atmosphere and ocean is done via the exchange of freshwater and heat fluxes, rather than by virtual salt fluxes. The terrestrial vegetation module of LOVECLIM, VECODE³⁸, computes the annual mean evolution of the vegetation cover based on annual mean values of several climatic variables.

Orbital-scale time-evolving ice-sheet boundary conditions in SIM are prescribed by changing ice-sheet orography and surface albedo. The corresponding anomalies were derived from the time-dependent ice-sheet reconstruction

obtained from the CLIMBER, 2b earth system model of intermediate complexity^{39,40}. Also, in LOVECLIM, the vegetation mask is adjusted to reflect time-evolving changes in ice-sheet-covered areas. Time-varying atmospheric greenhouse gas concentrations are prescribed in the model following greenhouse gas measurements from the EPICA DOME C ice core²⁴. Another important forcing considered here is orbitally induced insolation variations that are calculated from the algorithm of ref. 41. We employ an acceleration technique, which compresses the time-varying external boundary conditions by a factor of 5. Instead of running the coupled model for the entire period of 408,000 years^{42,43} the model experiment is 81,600 years long, while covering the entire forcing history of the last 408 thousand years. The acceleration technique is based on the assumption of relatively fast equilibration of surface variables to externally driven slow climate change. Through previous experimentation⁴² we have found that an acceleration factor of 5 is appropriate for the tasks envisioned here. Whereas, the climate model run follows closely the methodology of ref. 9, the current simulation uses a higher climate sensitivity, which amounts to $\sim 4^\circ\text{C}$ per CO_2 doubling. The result is a more realistic glacial/interglacial amplitude in surface temperatures compared to palaeo proxy data (see below).

To validate the model against palaeo proxy data we analyse 140 ka of the SIM model simulation (see below). This model simulation does not include the effects of millennial-scale variability associated with Dansgaard–Oeschger and Heinrich events. This will be added through a secondary model/data-based-procedure (see below).

While the full climate model simulation SIM covers 408 thousand years, only the last 125 thousand years are used to force the human dispersal model (see schematic Extended Data Fig. 1). The variables that are used as part of the climate forcing of the HDM are the simulated changes in temperature [$T_{\text{orb}}(x,y,t)$], net primary productivity [$N_{\text{orb}}(x,y,t)$] and desert fraction [$d_{\text{orb}}(x,y,t)$].

Validation of orbital-scale LOVECLIM simulation. To compare the transient LOVECLIM simulation SIM with palaeo proxy data, we conduct an empirical orthogonal function (EOF) analysis of the simulated sea surface temperatures (SST) from 140–0 ka and compare the resulting leading EOF pattern and corresponding principal component with an EOF analysis conducted on 63 palaeo proxy SST reconstructions^{25,44–89}. The SST reconstructions^{25,44–89} used for this analysis were required to cover the period from 140–10 ka. The location and the leading EOF pattern and corresponding principal component of these palaeo proxy data are shown in Extended Data Fig. 2. The model simulation reproduces both, the time evolution (Extended Data Fig. 2a) as well as the EOF pattern (Extended Data Fig. 2), in good agreement with the SST proxy data. We find higher EOF loadings for extratropical and some subtropical upwelling regions and somewhat damped EOF values for the tropical oceans. The resulting global mean SST time series which are based on the model and proxy EOF reconstructions (Extended Data Fig. 2c) exhibit a high degree of correlation and a similar magnitude for the transitions from the Last Glacial Maximum (LGM, 21 ka) to the early Holocene. However the magnitude of the Last Interglacial Ocean warming 130–120 ka is somewhat reduced in SIM, compared to the palaeo proxy reconstructions of global SST. There is also a reduction of the precessional (21 thousand year period) signal in the simulation relative to the palaeo data. Note that for this comparison we have made the assumption that annual mean SST in the model can be directly compared with a variety of SST proxies^{25,44–89} (such as alkenone, Mg/Ca and assemblage data). This requires that the proxies can be interpreted as an annual mean, which in some regions is not necessarily the case⁹⁰.

Other direct time series comparisons between simulated physical variables with palaeo proxy data are shown in Fig. 1. We find for instance that the magnitude as well as the timing of simulated surface temperatures over Antarctica in SIM matches the ice-core data well (Fig. 1e). Furthermore, the simulated hydroclimate variations in the Levant region bear close resemblance to orbital timescales with palaeo proxy reconstructions from speleothems (Fig. 1c) and lacustrine data (Fig. 1d).

To assess potential modelling uncertainties in hydroclimate for the selected time-slice of the LGM further we compare the simulated anomalies of the rainfall ratio between LGM and pre-industrial climate (relative to the pre-industrial values) in SIM with other CGCM LGM experiments conducted as part of the Palaeomodel Intercomparison Project, phase 3 (PMIP3). The results (Extended Data Fig. 3) clearly indicate that in spite of the fact that very similar boundary forcing conditions (greenhouse gas concentrations, ice-sheet topography and albedo and orbital forcing) are used, large modelling uncertainties exist in the simulated LGM rainfall patterns. Focusing on the particularly important human migration corridor of northern Africa, the LOVECLIM SIM experiment agrees well with the simulated drying in the CCSM4 and COSMOS-ASO simulations. In contrast the IPSL-CM5A-LR, GISS-E2-R and MPI-ESM-P models simulate significantly increased glacial rainfall over north Africa. For northern Europe, all CGCMs show

an overall drying for glacial conditions. The experimental design of PMIP3 does not include transient model experiments, so it is unclear at this stage, whether any of the other PMIP models would reproduce for example, the recorded hydroclimate variations over the past 125 thousand years in the Levant region (Fig. 1 d) in a qualitatively similar way as LOVECLIM.

Millennial-scale simulation and climate reconstruction. To account for the effects of millennial-scale Dansgaard–Oeschger (DO) and Heinrich events^{91,92} on climate and the resulting changes in human dispersal, we reconstructed the corresponding anomalies of surface temperature $T'_m(x,y,t)$, net primary productivity $N'_m(x,y,t)$ and desert fraction $d'_m(x,y,t)$, (where the subscript m stands for the millennial-scale climate anomalies and the prime symbol denotes the deviation from the long-term mean) using a previously conducted transient LOVECLIM climate model simulation⁹³, (abbreviated as MIL). This simulation is a climate model hindcast of the period 50–30 ka, which includes both orbital scale forcings (ice-sheets, greenhouse gas concentrations and orbital changes) and freshwater-forced millennial-scale climate shifts associated with each observed DO and Heinrich event during this period. For this climate model simulation we calculated the regression patterns $P_i(x,y)$ between the simulated Iberian Margin SST $T_{ib}^{sim}(t)$ and the corresponding spatiotemporal fields:

$$P_1(x,y) = \frac{\langle T_{ib}^{sim}(t)T'_m(x,y,t) \rangle}{\langle (T_{ib}^{sim})^2(t) \rangle}$$

$$P_2(x,y) = \frac{\langle T_{ib}^{sim}(t)N'_m(x,y,t) \rangle}{\langle (T_{ib}^{sim})^2(t) \rangle}$$

$$P_3(x,y) = \frac{\langle T_{ib}^{sim}(t)d'_m(x,y,t) \rangle}{\langle (T_{ib}^{sim})^2(t) \rangle}$$

To reconstruct the millennial-scale anomalies $[T_{m'}^*(x,y,t), N_{m'}^*(x,y,t), d_{m'}^*(x,y,t)]$ for the entire HDM period 130–0 ka, we multiply the model-based regression patterns with the observed high-pass-filtered Iberian margin SST variations²⁵ T_{ib}^{obs} that is, $T_{m'}^*(x,y,t) = T_{ib}^{obs}(t) P_1(x,y)$; $N_{m'}^*(x,y,t) = T_{ib}^{obs}(t) P_2(x,y)$; $d_{m'}^*(x,y,t) = T_{ib}^{obs}(t) P_3(x,y)$. The resulting millennial-scale anomaly maps were then added back to the corresponding fields of the orbital scale SIM simulation $[T_{orb}(x,y,t), N_{orb}(x,y,t), d_{orb}(x,y,t)]$. The comparison between reconstructed and observed Iberian Margin SST variability shows an excellent agreement, on both the orbital and millennial timescale (Fig. 1b). Furthermore, we find a good agreement on both timescales between reconstructed and simulated hydroclimate variations in the Levant region (Fig. 1d).

Climate forcing for HDM simulations. The full climate forcing (temperature, net primary productivity and desert fraction) of the HDM is provided by adding the directly simulated LOVECLIM variables from SIM $T_{orb}(x,y,t), N_{orb}(x,y,t), d_{orb}(x,y,t)$ to the reconstructed millennial-scale anomalies $T_{m'}^*(x,y,t), N_{m'}^*(x,y,t), d_{m'}^*(x,y,t)$, obtained from model/data-based linear regression reconstruction, which uses model-derived patterns of millennial-scale variability $P_1(x,y), P_2(x,y), P_3(x,y)$ from MIL, and a time series T_{ib}^{obs} of observed millennial-scale variability from an Iberian Margin sediment proxy SST reconstruction. This yields: $T(x,y,t) = T_{orb}(x,y,t) + bT_{m'}^*(x,y,t)$, $N(x,y,t) = N_{orb}(x,y,t) + bN_{m'}^*(x,y,t)$, $d(x,y,t) = d_{orb}(x,y,t) + bd_{m'}^*(x,y,t)$, where b in the standard HDM simulation is set to 1 (see Extended Data Fig. 1). To further test the effect of DO variability on human dispersal, we also conducted one experiment with $b=0$ (Fig. 3c). We also include the time-varying coastline into the HDM climate driving fields $T(x,y,t), N(x,y,t), d(x,y,t)$.

The orbital and millennial-scale contributions to temperature, net primary productivity and desert fraction can again be retrieved statistically through an Empirical Orthogonal Function (EOF) analysis of the fields $T(x,y,t), N(x,y,t), d(x,y,t)$. The resulting EOF patterns and principal components are depicted in Extended Data Figs 4–6. Because of the linear operations conducted, the EOF patterns of millennial-scale variability for the respective variables are very similar to the regression patterns $P_1(x,y), P_2(x,y), P_3(x,y)$ (not shown).

Transient HDM simulations. To quantify the effects of climate variability and human dispersal processes on the dispersal of *H. sapiens* during the Late Pleistocene, the HDM is run in various parameter configurations and for a number of realistic and more idealized climate scenarios.

Initialization and scenarios. All experiments start from the same initial *H. sapiens* density distribution in central Africa (see Fig. 2, upper left for pattern), representing idealized initial conditions 125 ka. The results are essentially insensitive to moderate 15 degree latitudinal and longitudinal shifts of the initial *H. sapiens* across central Africa. These initial dates are chosen to study how the prominent MIS5 precessionally paced openings of savannah-type corridors in northeastern Africa during HMW2 and 3 (Fig. 1) would have promoted the subsequent human dispersal out of Africa.

By integrating Equation (1) forward in time and using different climate scenarios (see Extended Data Table 2) for Net primary productivity ($N(x,y,t)$), desert fraction ($d(x,y,t)$), surface temperature ($T(x,y,t)$) and land–sea distribution, we can determine the effects of orbital-scale and millennial-scale climate variability on the simulated arrival times of *H. sapiens* in various regions (Fig. 3) for the different scenarios. The following forcing scenarios are chosen (see Extended Data Tables 1, 2):

(1) The standard early exit control run (scenario A) (see parameters in Extended Data Table 1, left column) simulates the evolution of *H. sapiens* for the past 125 thousand years in response to time varying $T(x,y,t), N(x,y,t), d(x,y,t)$, which includes orbital-scale and millennial-scale variability. Furthermore, to capture an increased adaptability to climate stressors we reduce the values of T_c and increase those for d_c linearly during the simulation (see Extended Data Table 1). Furthermore, the mobility of *H. sapiens* increases as a function of time in terms of diffusion and coastal advection speeds (Extended Data Table 1, left column). The results are shown in Fig. 2 and Fig. 3a. The Late Holocene value of $K=42 \text{ km}^2 \text{ year}^{-1}$ in this simulation is in the range of previous estimates^{31,33,94} for the Late Pleistocene *H. sapiens* and early- to mid-Holocene of $K=25\text{--}76 \text{ km}^2 \text{ year}^{-1}$. Our growth rate of 0.4% per year is a factor 3–4 smaller than previous estimates³². The simulated population range in scenario A for Europe during the LGM of 0.6 million individuals is about 3 times larger than a previous estimate⁹⁵.

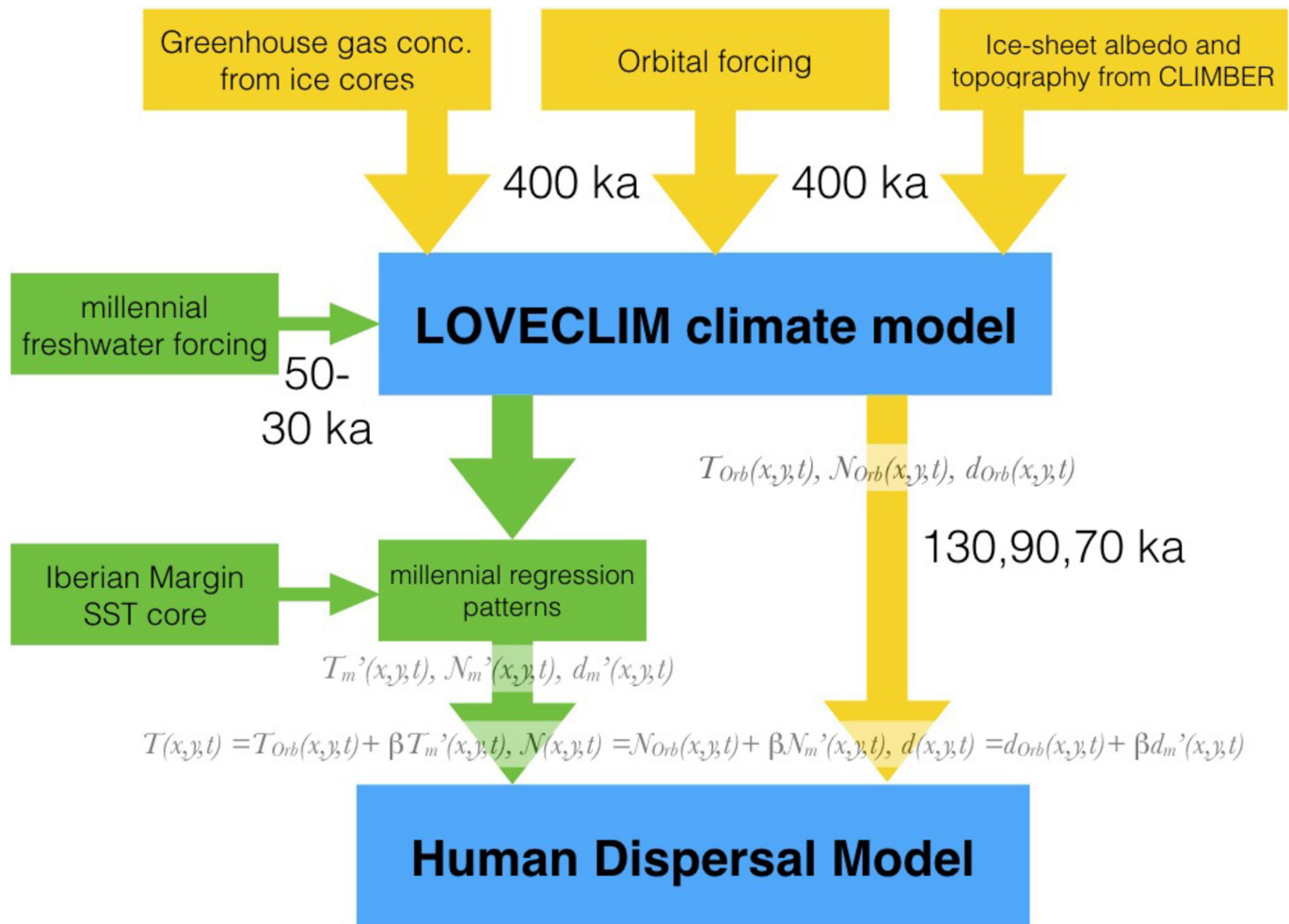
(2) The late exit (scenario B) uses the same overall configuration as Scenario A (including same initial condition), but different parameter values (see Extended Data Table 1, right column). The results are shown in Extended Data Fig. 7 and Fig. 3b. Most importantly, this scenario uses a higher sensitivity of human mortality to temperatures and a smaller initial diffusion rate.

(3) A 125 ka simulation (no DO), based on scenario A, with only orbital-scale forcing $T_{orb}(x,y,t), N_{orb}(x,y,t), d_{orb}(x,y,t)$ from SIM and without millennial-scale variability associated with Dansgaard–Oeschger and Heinrich events. The arrival time results are shown in Fig. 3c and some representative time series in Fig. 1, yellow lines.

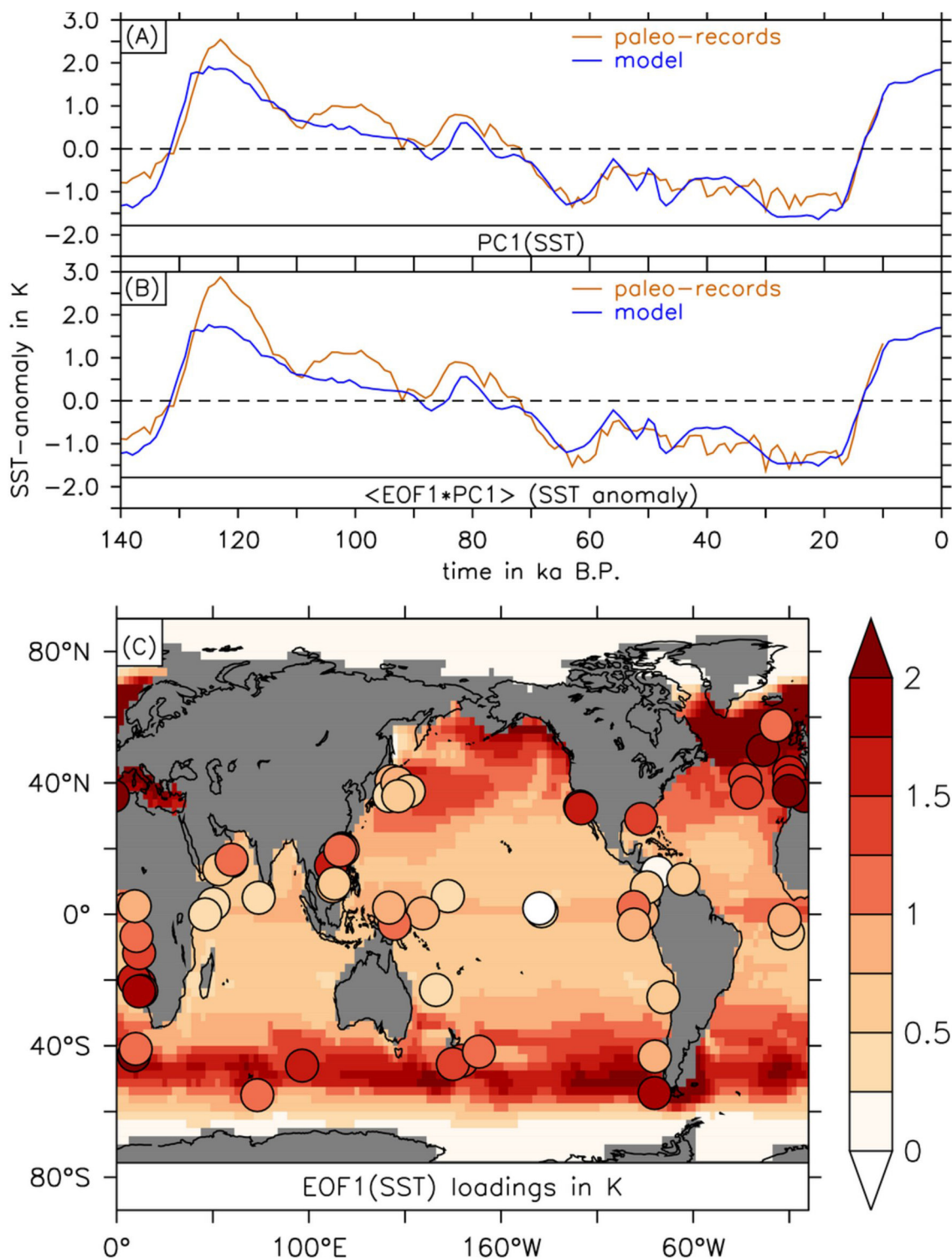
(4) Four 125 thousand-year-long HDM simulations using constant climate forcing $T_{orb}(x,y,t=t_c), N_{orb}(x,y,t=t_c), d_{orb}(x,y,t=t_c)$ with $t_c = 105, 70, 21$ ka using the same parameters as in scenario A. The arrival time results are shown in Fig. 3d–f. **Code availability.** The Matlab code of the human dispersion model is available upon request from the lead author.

- Young, D. A. & Bettinger, R. L. Simulating the Global Human Expansion in the Late Pleistocene. *J. Archaeol. Sci.* **22**, 89–92 (1995).
- Steele, J. Human dispersals: mathematical models and the archaeological record. *Hum. Biol.* **81**, 121–140 (2009).
- Fort, J., Pujol, T. & Cavalli-Sforza, L. L. Palaeolithic populations and waves of advance (Human range expansions). *Camb. Archaeol. J.* **14**, 53–61 (2004).
- Scerri, E. M. L., Groucutt, H. S., Jennings, R. P. & Petraglia, M. D. Unexpected technological heterogeneity in northern Arabia indicates complex Late Pleistocene demography at the gateway to Asia. *J. Hum. Evol.* **75**, 125–142 (2014).
- Goosse, H. *et al.* Description of the Earth system model of intermediate complexity LOVECLIM version 1.2. *Geosci. Model Dev.* **3**, 603–633 (2010).
- Opsteegh, J. D., Haarsma, R. J., Selten, F. M. & Kattenberg, A. ECBILT: a dynamic alternative to mixed boundary conditions in ocean models. *Tellus, Ser. A, Dyn. Meteorol. Oceanogr.* **50**, 348–367 (1998).
- Goosse, H. & Fichefet, T. Importance of ice–ocean interactions for the global ocean circulation: A model study. *Journal of Geophysical Research* **104**, 23337–23355 (1999).
- Brovkin, V., Ganopolski, A. & Svirezhev, Y. A continuous climate–vegetation classification for use in climate–biosphere studies. *Ecol. Modell.* **101**, 251–261 (1997).
- Ganopolski, A., Calov, R. & Claussen, M. Simulation of the last glacial cycle with a coupled climate ice-sheet model of intermediate complexity. *Clim. Past* **6**, 229–244 (2010).
- Ganopolski, A. & Calov, R. The role of orbital forcing, carbon dioxide and regolith in 100 kyr glacial cycles. *Clim. Past* **7**, 2391–2411 (2011).
- Berger, A. Long-term variations of caloric insolation resulting from the earth's orbital elements. *Quat. Res.* **9**, 139–167 (1978).
- Timm, O. & Timmermann, A. Simulation of the last 21000 years using accelerated transient boundary conditions. *J. Clim.* **20**, 4377–4401 (2007).
- Timm, O., Timmermann, A., Abe-Ouchi, A., Saito, F. & Segawa, T. On the definition of seasons in paleoclimate simulations with orbital forcing. *Paleoceanography* **23**, PA2221 (2008).
- Lawrence, K., Herbert, T., Brown, C., Raymo, M. & Haywood, A. High-amplitude variations in North Atlantic sea surface temperature during the early Pliocene warm period. *Paleoceanography* **24**, (2009).
- Naafls, B., Hefter, J. & Stein, R. Millennial-scale ice rafting events and Hudson Strait Heinrich-like Events during the late Pliocene and Pleistocene: a review. *Quat. Sci. Rev.* **80**, 1–28 (2013).
- Etourneau, J., Martinez, P., Blanz, T. & Schneider, R. Pliocene–Pleistocene variability of upwelling activity, productivity, and nutrient cycling in the Benguela region. *Geology* **37**, 871–874 (2009).

47. Herbert, T. D., Peterson, L. C., Lawrence, K. T. & Liu, Z. Tropical ocean temperatures over the past 3.5 million years. *Science* **328**, 1530–1534 (2010).
48. Li, L. *et al.* A 4-Ma record of thermal evolution in the tropical western Pacific and its implications on climate change. *Earth Planet. Sci. Lett.* **309**, 10–20 (2011).
49. de Garidel-Thoron, T., Rosenthal, Y., Bassinot, F. & Beaufort, L. Stable sea surface temperatures in the western Pacific warm pool over the past 1.75 million years. *Nature* **433**, 294–298 (2005).
50. Medina-Elizalde, M. & Lea, D. W. The mid-Pleistocene transition in the tropical Pacific. *Science* **310**, 1009–1012 (2005).
51. Russon, T. *et al.* Inter-hemispheric asymmetry in the early Pleistocene Pacific warm pool. *Geophys. Res. Lett.* **37**, (2010).
52. Pisias, N. & Rea, D. Late pleistocene paleoclimatology of the central equatorial Pacific: sea surface response to the southeast trade winds. *Paleoceanography* **3**, 21–37 (1988).
53. Liu, Z. & Herbert, T. D. High-latitude influence on the eastern equatorial Pacific climate in the early Pleistocene epoch. *Nature* **427**, 720–723 (2004).
54. Schaefer, G. *et al.* Planktic foraminiferal and sea surface temperature record during the last 1 Myr across the Subtropical Front, Southwest Pacific. *Mar. Micropaleontol.* **54**, 191–212 (2005).
55. Hayward, B. *et al.* The effect of submerged plateaux on Pleistocene gyral circulation and sea-surface temperatures in the Southwest Pacific. *Global Planet. Change* **63**, 309–316 (2008).
56. Martínez-García, A., Rosell-Melé, A., McClymont, E. L., Gersonde, R. & Haug, G. H. Subpolar link to the emergence of the modern equatorial Pacific cold tongue. *Science* **328**, 1550–1553 (2010).
57. Salgueiro, E. *et al.* Temperature and productivity changes off the western Iberian margin during the last 150 ky. *Quat. Sci. Rev.* **29**, 680–695 (2010).
58. Martínez, J., Mora, G. & Barrows, T. Paleocceanographic conditions in the western Caribbean Sea for the last 560 kyr as inferred from planktonic foraminifera. *Mar. Micropaleontol.* **64**, 177–188 (2007).
59. Voelker, A. H. & de Abreu, L. in *Abrupt Climate Change: Mechanisms, Patterns, and Impacts* Vol. 193 (eds Rashid, H., Polyak, L. & Mosley-Thompson, E.) (AGU, Geophysical Monograph Series, 2011).
60. Ziegler, M., Nurnberg, D., Karas, C., Tiedemann, R. & Lourens, L. Persistent summer expansion of the Atlantic Warm Pool during glacial abrupt cold events. *Nat. Geosci.* **1**, 601–605 (2008).
61. Herbert, T. D. & Schuffert, J. D. Vol. 165 1–9 (Proceedings of the Ocean Drilling Program, Scientific Results, College Station, TX (Ocean Drilling Program), 2000).
62. Calvo, E., Villanueva, J., Grimalt, J., Boelaert, A. & Labeyrie, L. New insights into the glacial latitudinal temperature gradients in the North Atlantic. Results from U-37(K') sea surface temperatures and terrigenous inputs. *Earth Planet. Sci. Lett.* **188**, 509–519 (2001).
63. Weldeab, S., Lea, D. W., Schneider, R. R. & Andersen, N. 155,000 years of West African monsoon and ocean thermal evolution. *Science* **316**, 1303–1307 (2007).
64. Mix, A. C. & Fairbanks, R. G. North-Atlantic surface-ocean control of pleistocene deep-ocean circulation. *Earth Planet. Sci. Lett.* **73**, 231–243 (1985).
65. Martrat, B. *et al.* Abrupt temperature changes in the Western Mediterranean over the past 250,000 years. *Science* **306**, 1762–1765 (2004).
66. Schneider, R. R., Mueller, P. J. & Ruhland, G. Late quaternary surface circulation in the east Equatorial South-Atlantic - evidence from alkenone sea-surface temperatures. *Paleoceanography* **10**, 197–219 (1995).
67. Kirst, G., Schneider, R., Muller, P., von Storch, I. & Wefer, G. Late Quaternary temperature variability in the Benguela Current System derived from alkenones. *Quat. Res.* **52**, 92–103 (1999).
68. Nurnberg, D., Muller, A. & Schneider, R. Paleo-sea surface temperature calculations in the equatorial east Atlantic from Mg/Ca ratios in planktic foraminifera: A comparison to sea surface temperature estimates from U-37(K'), oxygen isotopes, and foraminiferal transfer function. *Paleoceanography* **15**, 124–134 (2000).
69. Budziak, D. in *Berichte aus dem Fachbereich Geowissenschaften der Universität Bremen* Vol. **170** 114pp (2000).
70. Bard, E., Rostek, F. & Sonzogni, C. Interhemispheric synchrony of the last deglaciation inferred from alkenone palaeothermometry. *Nature* **385**, 707–710 (1997).
71. Pelejero, C., Grimalt, J., Heilig, S., Kienast, M. & Wang, L. High-resolution U-37(K) temperature reconstructions in the South China Sea over the past 220 kyr. *Paleoceanography* **14**, 224–231 (1999).
72. Wei, G., Deng, W., Liu, Y. & Li, X. High-resolution sea surface temperature records derived from foraminiferal Mg/Ca ratios during the last 260 ka in the northern South China Sea. *Palaeogeogr. Palaeoclimatol. Palaeoecol.* **250**, 126–138 (2007).
73. Oppo, D. & Sun, Y. Amplitude and timing of sea-surface temperature change in the northern South China Sea: dynamic link to the East Asian monsoon. *Geology* **33**, 785–788 (2005).
74. Koizumi, I. & Yamamoto, H. Paleocceanographic evolution of North Pacific surface water off Japan during the past 150,000 years. *Mar. Micropaleontol.* **74**, 108–118 (2010).
75. Dyez, K. & Ravelo, A. Late Pleistocene tropical Pacific temperature sensitivity to radiative greenhouse gas forcing. *Geology* **41**, 23–26 (2013).
76. Tachikawa, K., Timmermann, A., Vidal, L., Sonzogni, C. & Timm, O. CO₂ radiative forcing and Intertropical Convergence Zone influences on western Pacific warm pool climate over the past 400 ka. *Quat. Sci. Rev.* **86**, 24–34 (2014).
77. Jasper, J. P., Hayes, J. M., Mix, A. C. & Prah, F. G. Photosynthetic fractionation of ¹³C and concentrations of dissolved CO₂ in the central equatorial Pacific during the last 255,000 years. *Paleoceanography* **9**, 781–798 (1994).
78. Yu, P. *et al.* Influences of extratropical water masses on equatorial Pacific cold tongue variability during the past 160 ka as revealed by faunal evidence of planktic foraminifers. *J. Quaternary Sci.* **27**, 921–931 (2012).
79. Ho, S. *et al.* Sea surface temperature variability in the Pacific sector of the Southern Ocean over the past 700 kyr. *Paleoceanography* **27**, (2012).
80. Rincon-Martinez, D. *et al.* More humid interglacials in Ecuador during the past 500 kyr linked to latitudinal shifts of the equatorial front and the Intertropical Convergence Zone in the eastern tropical Pacific. *Paleoceanography* **25**, (2010).
81. Herbert, T. D. *et al.* Collapse of the California Current during glacial maxima linked to climate change on land. *Science* **293**, 71–76 (2001).
82. Lea, D. W., Pak, D. K. & Spero, H. J. Climate impact of late quaternary equatorial Pacific sea surface temperature variations. *Science* **289**, 1719–1724 (2000).
83. Yamamoto, M., Yamamoto, M. & Tanaka, Y. The California current system during the last 136,000 years: response of the North Pacific High to precessional forcing. *Quat. Sci. Rev.* **26**, 405–414 (2007).
84. Cortese, G., Abelmann, A. & Gersonde, R. A glacial warm water anomaly in the subantarctic Atlantic Ocean, near the Agulhas Retroflection. *Earth Planet. Sci. Lett.* **222**, 767–778 (2004).
85. Becquey, S. & Gersonde, R. A 0.55-Ma paleotemperature record from the Subantarctic zone: Implications for Antarctic Circumpolar Current development. *Paleoceanography* **18**, (2003).
86. Sowers, T. *et al.* A 135,000-year Vostok-specmap common temporal framework. *Paleoceanography* **8**, 737–766 (1993).
87. Pichon, J. *et al.* Surface water temperature changes in the high latitudes of the southern hemisphere over the last glacial-interglacial cycle. *Paleoceanography* **7**, 289–318 (1992).
88. Sikes, E., Howard, W., Neil, H. & Volkman, J. Glacial-interglacial sea surface temperature changes across the subtropical front east of New Zealand based on alkenone unsaturation ratios and foraminiferal assemblages. *Paleoceanography* **17**, (2002).
89. Pahnke, K. & Sachs, J. Sea surface temperatures of southern midlatitudes 0–160 kyr BP. *Paleoceanography* **21**, (2006).
90. Timmermann, A., Sachs, J. & Timm, O. E. Assessing divergent SST behavior during the last 21 ka derived from alkenones and G. ruber-Mg/Ca in the equatorial Pacific. *Paleoceanography* **29**, 680–696 (2014).
91. Masson-Delmotte, V. *et al.* 383–464 (Cambridge University Press, 2013).
92. Sepulchre, P. *et al.* H4 abrupt event and late Neanderthal presence in Iberia. *Earth Planet. Sci. Lett.* **258**, 283–292 (2007).
93. Menviel, L., Timmermann, A., Friedrich, T. & England, M. H. Hindcasting the continuum of Dansgaard-Oeschger variability: mechanisms, patterns and timing. *Clim. Past* **10**, 63–77 (2014).
94. Pinhasi, R., Fort, J. & Ammerman, A. J. Tracing the origin and spread of agriculture in Europe. *PLoS Biol.* **3**, e410 (2005).
95. Tallavaara, M., Luoto, M., Korhonen, N., Järvinen, H. & Seppä, H. Human population dynamics in Europe over the Last Glacial Maximum. *Proc. Natl Acad. Sci. USA* **112**, 8232–8237 (2015).

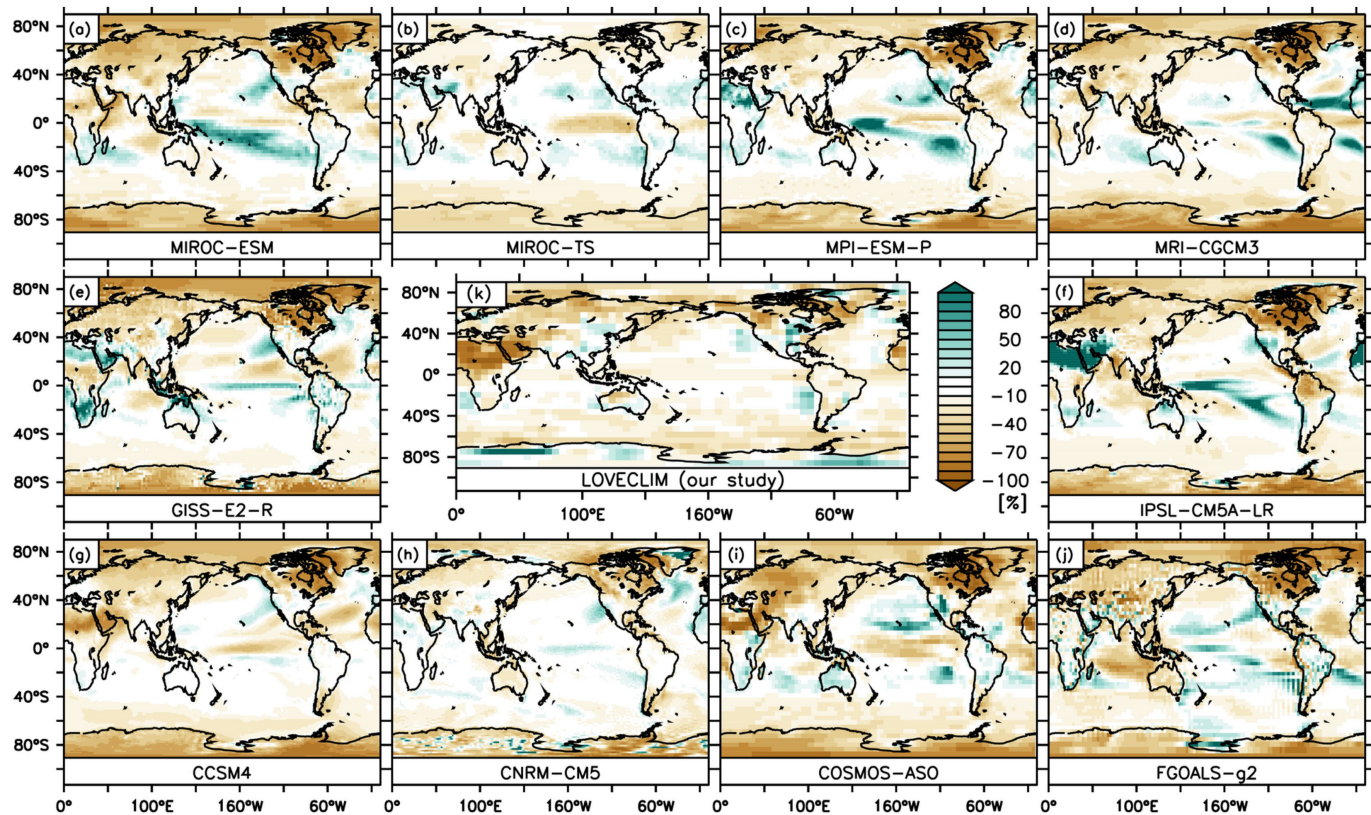


Extended Data Figure 1 | Schematics of modelling framework adopted for this study.



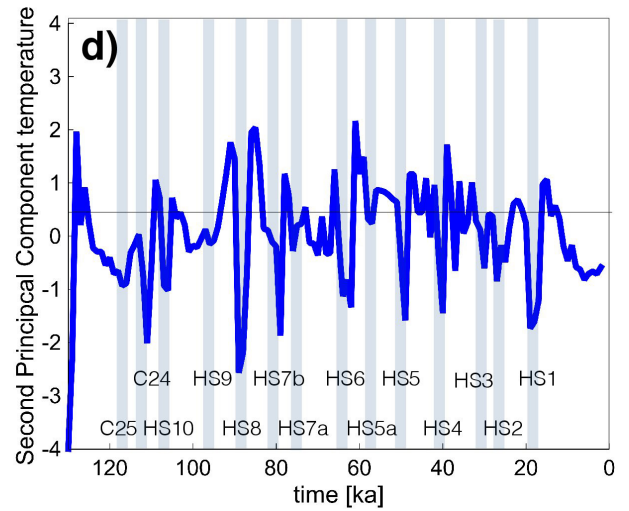
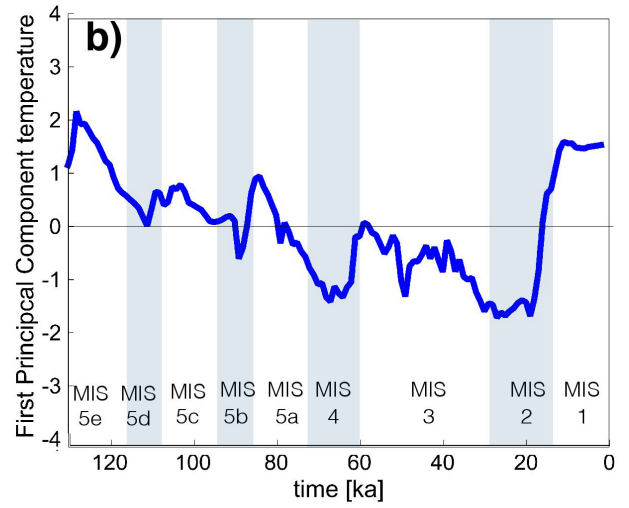
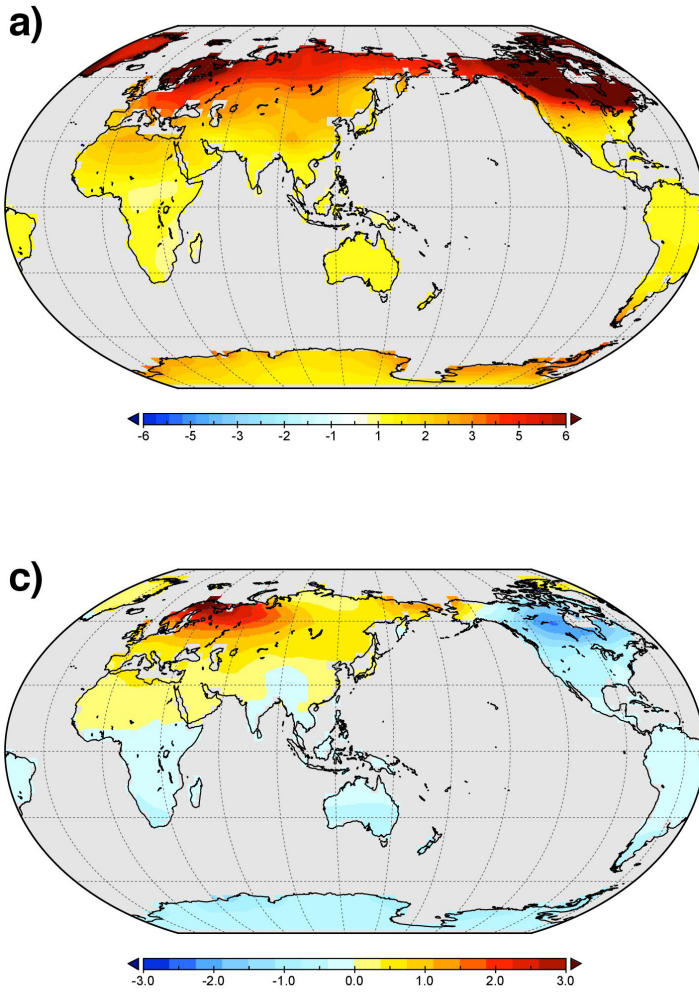
Extended Data Figure 2 | Validation of climate model simulation for temperature with palaeo sea surface temperature (SST) reconstructions. Pattern and temporal evaluation of leading Empirical Orthogonal Function (EOF1) of reconstructed and simulated SST. **a**, Principal components of the EOF1 (PC1) for SST from 63 palaeo-

records^{25,44–89} (orange) covering the period 140–10 ka and simulated SST (blue) using every model grid point. **b**, Globally-averaged SST anomaly (K) from EOF1-based reconstruction. Colours as in **a**. **c**, EOF1-pattern (K) for 63 palaeo records^{25,44–89} (circles) and for simulated SST in global domain (shading).



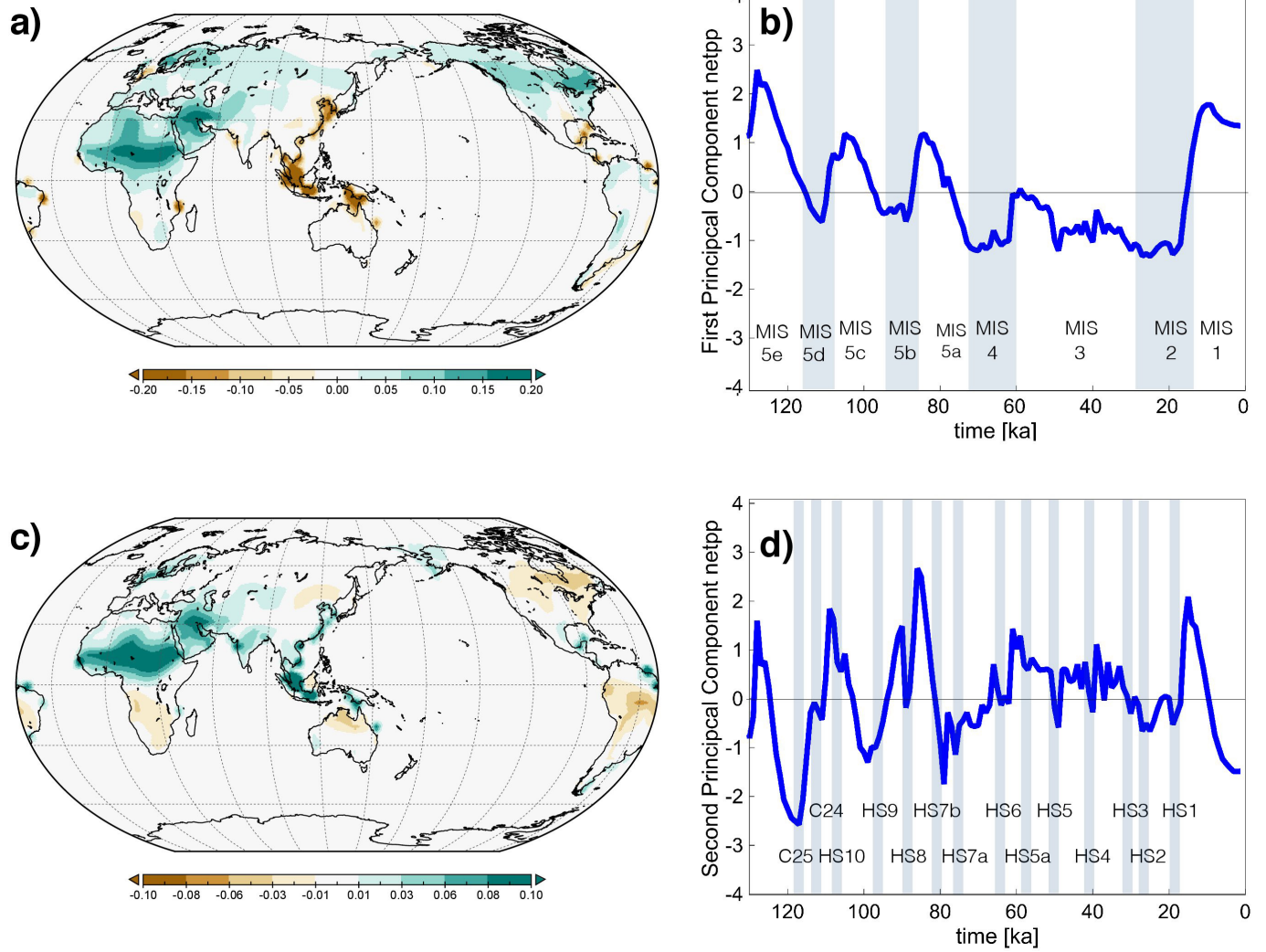
Extended Data Figure 3 | Comparison of LOVECLIM simulation with other PMIP3 CGCM Last Glacial Maximum simulations. a–j, Simulated annual mean rainfall differences (LGM versus pre-industrial) relative to the pre-industrial long-term annual mean rainfall (%) for ten different climate model simulations (MIROC-ESM (a), MIROC-TS (b), MPI-ESM-P (c),

MRI-CGCM3 (d), GISS-E2-R (e), IPSL-CM5A-LR (f), CCSM4 (g), CNRM-CM5 (h), COSMOS-ASO (i) and FGOALS-g2 (j)) conducted as part of the Paleo Model Intercomparison Project, Phase 5 (PMIP5) (see Methods) and the LOVECLIM model (k) used here.

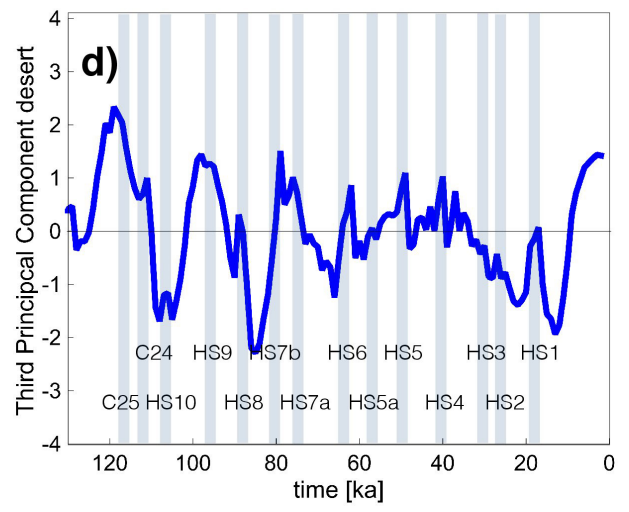
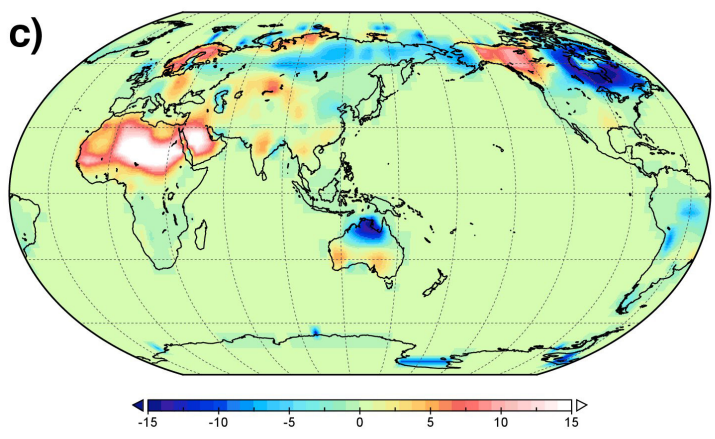
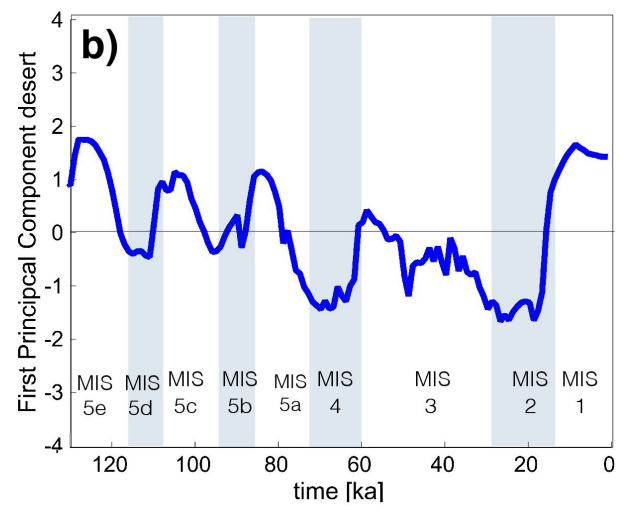
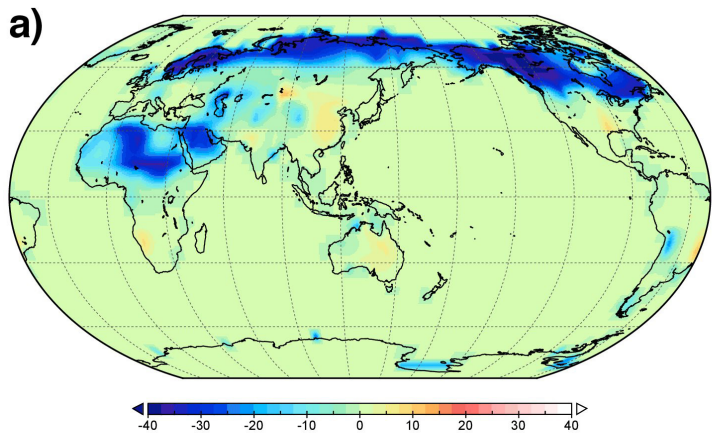


Extended Data Figure 4 | Temperature forcing for HDM. **a**, First empirical orthogonal function (EOF) of temperature (°C). **b**, The corresponding principal component. First EOF mode captures orbital-scale variability. **c**, Second empirical orthogonal function of temperature (°C). The

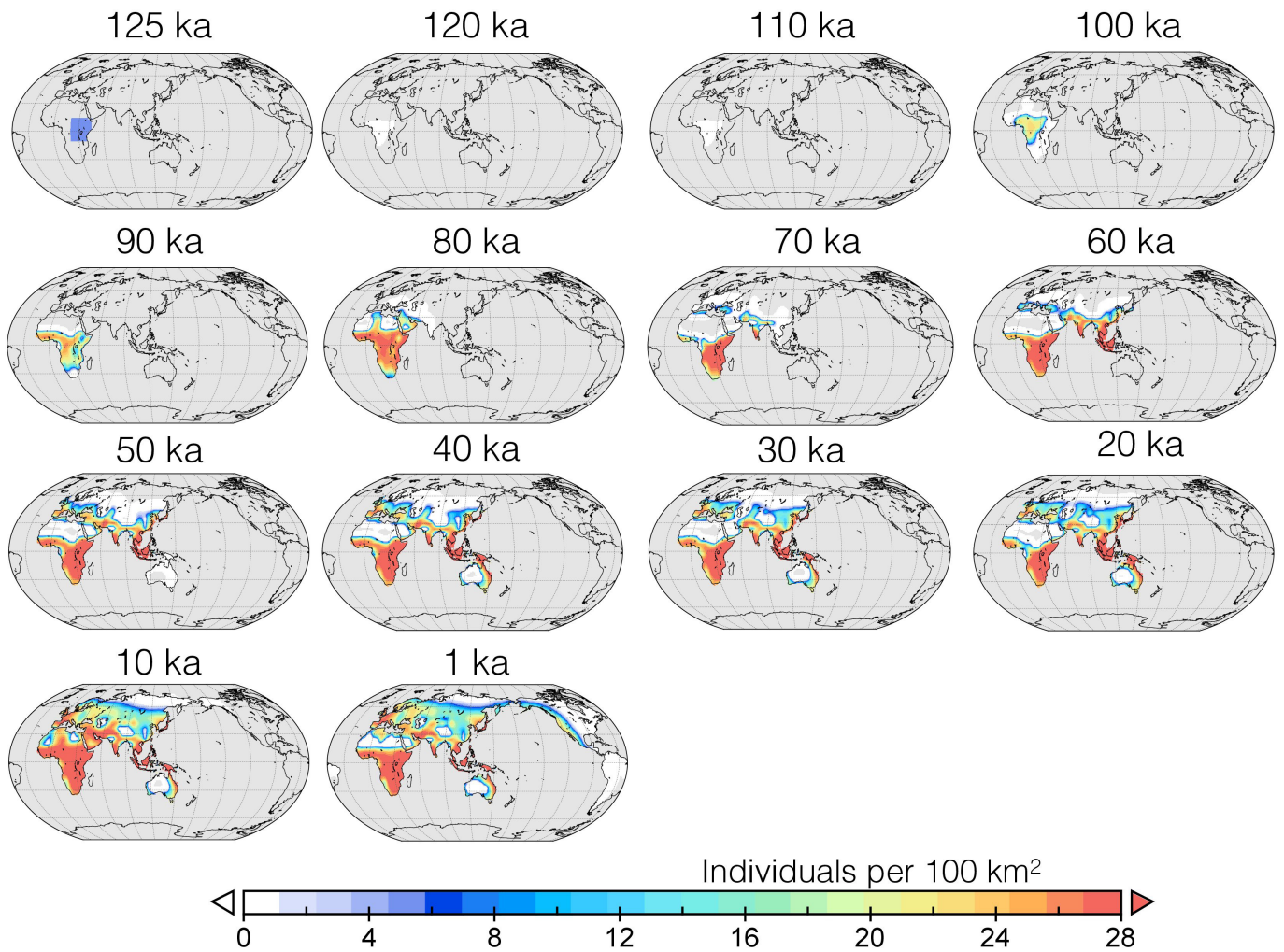
corresponding principal component is shown in **d**. Second EOF mode captures Heinrich and Dansgaard–Oeschger events. In **b**, the main Marine Isotope Stages (MIS) are indicated with blue shading. In **d**, the blue shading indicates the main Heinrich stadials and the C-events.



Extended Data Figure 5 | Net primary production forcing for HDM. Same as Extended Data Fig. 4, but for primary production ($\text{kgC m}^{-2} \text{yr}^{-1}$).



Extended Data Figure 6 | Desert fraction forcing for HDM. Same as Extended Data Fig. 4, but for desert fraction (%).



Extended Data Figure 7 | Late Pleistocene human dispersal. Snapshots of the simulated evolution of human density (individuals per 100 km²) over the past 125 ka using the parameters of the scenario B (late exit) experiment (see Methods) with full climate (orbital and millennial-scale) and sea level forcing and with human adaptation.

Extended Data Table 1 | Parameter configurations of human dispersal model used in early exit (scenario A) and late exit (scenario B) scenarios

Parameter	Early exit scenario	Late exit scenario
K (main diffusion parameter)	4.25 km ² year ⁻¹ to 42 km ² year ⁻¹ over 125 ka	2.125 km ² year ⁻¹ to 42 km ² year ⁻¹ over 125 ka
T _w (Temperature width)	6 °C	7 °C
T _c (critical temperature)	15 °C to -35 °C over 125 ka	17.5 °C to -35 °C over 125 ka
d _w (Desert width)	8%	8%
d _c (critical desert fraction)	45- 70% over 125 ka	45- 80% over 125 ka
N _c (critical net primary productivity)	0.1 kgC/m ² /year	0.1 kgC/m ² /year
N _w (net primary productivity width)	0.3 kgC/m ² /year	0.3 kgC/m ² /year
G (Growth rate)	0.004 year ⁻¹	0.004 year ⁻¹
m (Mortality rate)	0.105 year ⁻¹	0.105 year ⁻¹
a (nonlinear damping rate)	1.25 10 ⁻⁶ year ⁻¹	1.25 10 ⁻⁶ year ⁻¹
U _p (coastal propagation speed)	0.0687 to 2.4056 km year ⁻¹ over 125 ka	0.0343 to 2.0619 km year ⁻¹ over 125 ka

Extended Data Table 2 | Sensitivity experiments conducted with human dispersal model using different climate and dispersal scenarios

Abbreviation	Forcings and experimental set-up
Scenario A (Early exit)	Fully varying climate and sea level conditions 125-0 ka: $T(x,y,t)$, $N(x,y,t)$, $d(x,y,t)$, parameters in Extended Table 1, left column
noDO	Varying orbital-scale climate and sea level conditions 125-0 ka: $T_{orb}(x,y,t)$, $N_{orb}(x,y,t)$, $d_{orb}(x,y,t)$, parameters in Extended Table 1, left column
Scenario B (Late exit)	Fully varying climate and sea level conditions 125-0 ka: $T(x,y,t)$, $N(x,y,t)$, $d(x,y,t)$, parameters in Extended Table 1, right column
105 ka	Perpetual 105 ka climate and sea level conditions for 125,000 simulation years: $T_{orb}(x,y,105 ka)$, $N_{orb}(x,y,105 ka)$, $d_{orb}(x,y,105 ka)$, parameters in Extended Table 1, left column
70 ka	Perpetual 70 ka climate and sea level conditions for 125,000 simulation year: $T_{orb}(x,y,70 ka)$, $N_{orb}(x,y,70 ka)$, $d_{orb}(x,y,70 ka)$, parameters in Extended Table 1, left column
21 ka	Perpetual 21 ka climate and sea level conditions for 125,000 simulation years: $T_{orb}(x,y,21 ka)$, $N_{orb}(x,y,21 ka)$, $d_{orb}(x,y,21 ka)$, parameters in Extended Table 1, left column